Two-dimensional Ekman-Inertial Instability: A comparison with Inertial Instability

By

Fabiola Trujano-Jiménez[1] (fabiola.trujanojimenez@mail.utoronto.ca)

Varvara E. Zemskova[2,3] (bzemskov@uwaterloo.ca)

Nicolas Grisouard[1] (nicolas.grisouard@utoronto.ca)

[1] Department of Physics, University of Toronto, Toronto, ON M5S 1A7, Canada

[2] Department of Applied Mathematics, University of Waterloo, Waterloo, ON N2L 3G1, Canada

[3] College of Earth, Ocean, and Atmospheric Sciences, Oregon State University, Oregon 97331, USA

Two-dimensional Ekman-Inertial Instability:
a comparison with Inertial Instability

Fabiola Trujano-Jiménez,[1] Varvara E. Zemskova,[2,3] and Nicolas Grisouard[1,*]
[1] *Department of Physics, University of Toronto, Toronto, ON M5S 1A7, Canada*
[2] *Department of Applied Mathematics, University of Waterloo, Waterloo, ON N2L 3G1, Canada*
[3] *College of Earth, Ocean, and Atmospheric Sciences, Oregon State University, Oregon 97331, USA*

(Dated: February 3, 2025)

In the ocean, submesoscale flows tend to undergo several hydrodynamic instabilities. In particular, Inertial Instability (InI) and Ekman-Inertial Instability (EII) are known to develop in geostrophically balanced barotropic flows whose lateral shear is larger in magnitude and opposite in sign to the Coriolis parameter. Although these instabilities share some elements, their dynamical nature can lead to fundamental differences. However, the current analytical description of EII is one-dimensional, which makes it difficult to compare against InI in a more realistic scenario. To overcome this limitation, we conduct two-dimensional numerical simulations of both InI and EII in a submesoscale jet and explore the induced vertical flow, the growth rate, and the energetics of each instability. Furthermore, we investigate the sensitivity of our results to variations in the minimum Rossby number of the jet. We find that EII grows faster than InI and induces stronger vertical flow, especially near the surface. Both instabilities radiate inertial waves away from the current, and these waves predominantly propagate across the anticyclonic side of the jet. Finally, when the instabilities weaken, the fluid reaches a stable state that is remarkably similar in both cases. This study highlights the similarities and differences between InI and EII and provides further insight into the mechanism behind EII that makes it capable of outcompeting other submesoscale instabilities.

I. INTRODUCTION

The dynamics of the ocean are shaped by physical processes of different temporal and spatial scales, as well as by the complex interactions between them [1, 2]. In recent decades, special attention has been drawn to the submesoscale, an ocean scale characterized by flows with horizontal scales of $0.1 - 10$ km, vertical scales of $0.001 - 1$ km, and temporal scales of hours to days [3, 4]. The increasing availability of high-resolution computational models and remote sensing instruments led to the emergence of the submesoscale as a field of study and demonstrated its remarkable relevance in connecting larger scales such as the mesoscale and smaller scales such as the microscale.

Submesoscale flows induce relatively strong vertical velocities, making them essential for transporting momentum, heat, gases, and nutrients between the surface and the interior of the ocean [5–10]. For this reason, submesoscale flows play a crucial role not only in ocean dynamics, but also in the global climate system and the sustenance of marine life. Moreover, such intense vertical flows provide a path for dissipation of kinetic energy by transferring energy from large to small scales in a process known as a forward cascade of energy [3, 11, 12]. In the mesoscale, most of the kinetic energy is stored in the form of jets and eddies that are approximately in geostrophic and hydrostatic balance. Their kinetic energy tends to experience an inverse cascade, i.e., energy transfers from smaller to larger scales, and they tend to be robust to disturbances without experiencing significant dissipation. As such, submesoscale flows are proving to be an essential link to closing the kinetic energy budget of the ocean [13].

The submesoscale is characterized by Rossby numbers ($\mathrm{Ro} = \zeta/f$, where ζ is the vertical vorticity and f is the Coriolis parameter) of $O(1)$ [3, 14]. This regime makes submesoscale jets particularly prone to becoming dynamically unstable. Observational data from a survey conducted offshore of the Gulf Stream, with a resolution of $O(1\text{ km})$, evidenced the ubiquity of the $Ro \sim 1$ regime in the upper ocean [15], where several submesoscale instabilities can develop [16–23]. In particular, when submesoscale barotropic flows in geostrophic balance satisfy the condition $\mathrm{Ro} < -1$, small perturbations draw energy from the lateral shear of the flow and can grow enough to break the balance. This process is known as Inertial Instability (InI) and has been thought to play an important role in submesoscale dynamics [22, 24, 25]. In fact, linear stability analysis in infinite and uniform domains in the inviscid regime predicts that plane wave-like perturbations grow at a rate of $|f|\sqrt{-1 - \mathrm{Ro}}$. Note that this type of analysis implicitly assumes that there is no interaction between different modes; in reality, such interactions could lead to much faster growth rates shortly after the onset of the instability [26].

---

[*] nicolas.grisouard@utoronto.ca

Under the same conditions for InI development, along with the fact that the flow undergoes a sudden change in the surface wind stress, Grisouard and Zemskova [27] revealed the existence of what could be considered either a particular manifestation of InI, or a new submesoscale instability: the Ekman-Inertial Instability (EII). Similarly to InI, EII develops in submesoscale flows with $\mathrm{Ro} < -1$, and similarly to an Ekman layer, it is triggered by a tangential stress on the surface.

Despite the similarities previously described, there are several features that make EII a distinct instability capable of competing against and even grow faster than other common submesoscale instabilities. Indeed, one of the main differences between EII and InI is found in their respective triggering mechanisms. InI typically develops from perturbations in the interior of the flow, and hence, it is often described by vertical modes and studied using plane-wave linear stability analysis. In contrast, the perturbation that causes EII is a mismatch between surface and interior tangential stresses, which in turn propagates toward deeper layers of the flow via viscous tangential fluxes. This results in a very different growth rate for both instabilities. Namely, traditional linear stability analysis shows that InI grows exponentially, with the growth rate reduced by viscosity [e.g., 25, 28]. On the contrary, for a fluid layer at a given depth and a fast enough surface disturbance, EII exhibits a super-exponential growth rate in the first stage of its development when viscous stresses provide momentum from above. The EII growth rate then rapidly decreases and reaches a minimum below the inertial value, when said layer now provides momentum to the layer below. Eventually, the EII growth rate slowly tends toward the exponential growth rate of InI. As a result, a fundamental difference is found in the sources of energy and the effects of the turbulent viscosity in each instability. The only source of energy for InI is in the lateral shear of the flow, whereas viscous effects counteract its development throughout the entire process. On the contrary, in EII viscous stresses initially provide kinetic energy to a given layer of fluid, enhancing the development of EII during its early stages [27]. In later stages, viscous stresses then revert to their more standard behavior of slowing down the growth of the perturbations.

The analytical solution of Grisouard and Zemskova [27] for EII applies to a one-dimensional column of fluid. Consequently, this description neglects horizontal variations of the Rossby number, which implies an endless source of unstable flow since the Rossby number would indefinitely satisfy the condition $\mathrm{Ro} < -1$. In a more realistic scenario, as the instability develops, the Rossby number will vary across the flow, and the mixing of stable and unstable flow will eventually cause the instability to weaken and fade away. In order to account for this effect, an additional dimension must be included. This work aims to expand our current understanding of EII with a detailed analysis of the similarities and differences with the closely-related InI, using an idealized model of a two-dimensional submesoscale current. Although in the real ocean submesoscale instabilities take place in more complicated scenarios, a more realistic model would make it difficult to disentangle EII from other submesoscale processes. Also, Grisouard and Zemskova [27] found that EII has the potential to grow significantly faster compared with InI, but also with instabilities for which baroclinicity is a key ingredient, such as symmetric or baroclinic instability. It could play a key role before these other instabilities have had time to act. As the wind stress often changes at the ocean surface, a study to examine the effects of EII is relevant, especially as these processes occur on such small spatio-temporal scales that might make it difficult to observe in the ocean.

The structure of this paper is as follows. In section II, we introduce the details of our numerical setup and the growth rate and energetics analysis performed on our data. Section III presents the results of a sample simulation, followed by a discussion on their sensitivity to variations in the Rossby number. We discuss the limitations and future perspectives of our study and summarize our findings in section IV.

II. METHODOLOGY

A. Numerical Setup

We set up a jet-like current of typical half-width $L = 1$ on an f-plane Cartesian ($\hat{\boldsymbol{x}}$, $\hat{\boldsymbol{y}}$, $\hat{\boldsymbol{z}}$, with $\hat{\boldsymbol{z}}$ pointing vertically upward) nondimensional domain of horizontal length $L_x = 16$ and height $H = 1$. The jet flows in the $\hat{\boldsymbol{y}}$ direction. Strictly speaking, the domain is two-and-a-half-dimensional, namely, there can be a non-zero velocity in the y-direction, but we set all y-derivatives to zero. Since we loosely draw inspiration from the mixed layer of the upper ocean, as a first step approach, our model uses the equations of motion for a constant-density flow, which is a rough approximation thereof. Also, at least in the case of EII, lateral buoyancy gradients are laterally advected like passive tracers, and do not play a leading role in the dynamics [27]. The unit time scale is the inverse of the Coriolis parameter $1/f = 1$. Then, the nondimensionalized equations of motion take the form

$$\frac{D\boldsymbol{v}}{Dt} + f\hat{\boldsymbol{z}} \times \boldsymbol{v} + \nabla\phi = \mathrm{Ek}\nabla^2\boldsymbol{v} \quad \text{and} \quad \nabla \cdot \boldsymbol{v} = 0, \tag{1}$$

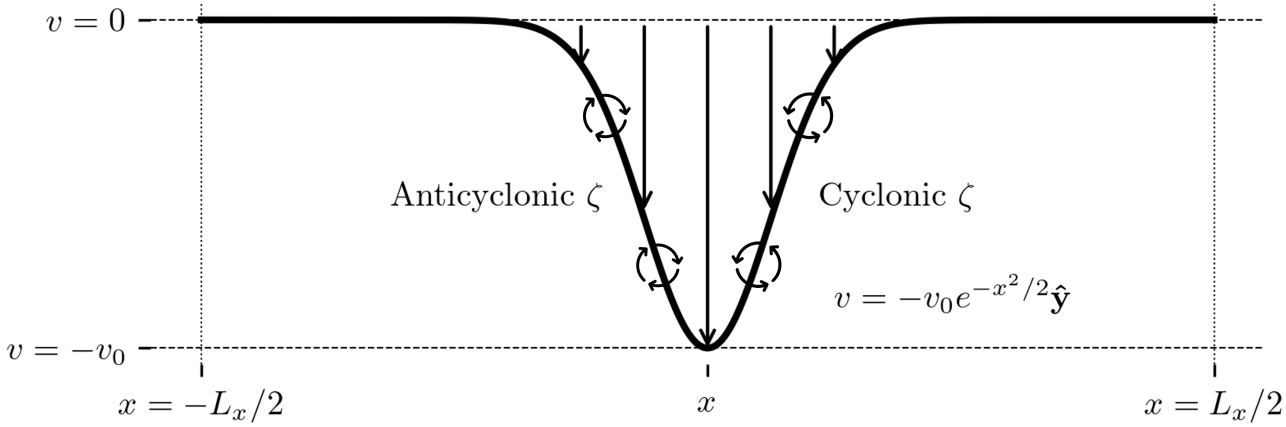

FIG. 1. Top view of numerical setup showing regions of anticyclonic and cyclonic vorticity $\zeta = \partial_x v$, with the shape of the current modeled as in Eq. (2).

where $\boldsymbol{v} = u\hat{\boldsymbol{x}} + v\hat{\boldsymbol{y}} + w\hat{\boldsymbol{z}}$ is the velocity field and its Cartesian components, ϕ includes the pressure deviations from hydrostatic balance divided by the fluid density, as well as the centrifugal potential, and $\mathrm{Ek} = \nu/fH^2$ is the Ekman number, with ν the kinematic viscosity. Note that as mentioned above, $f = 1$ in our nondimensional unit system, but we keep its symbol to keep track of the Coriolis terms.

The initial state of the current is modeled as a Gaussian function given by

$$\boldsymbol{v}|_{t=0} = -v_0 \mathrm{e}^{-x^2/2}\hat{\boldsymbol{y}}, \tag{2}$$

where $v_0 = -\mathrm{Ro}_{\min}\mathrm{e}^{1/2}$ is the amplitude of the current. Note that $\mathrm{Ro}_{\min} = \min(\mathrm{Ro})$, with $\mathrm{Ro} = \partial_x v/f$ in our two-dimensional model. This current is a crude model for submesoscale jets that are generated during the frontogenesis process, typically due to strain from mesoscale eddies [3]. Once generated, these jets are prone to instabilities, two of which are the focus of this study. A sketch of the current is depicted in Figure 1.

We apply a constant wind stress τ in the direction of the initial current, that is,

$$\partial_z u|_{z=0} = 0 \quad \text{and} \quad \partial_z v|_{z=0} = \tau. \tag{3}$$

It is important to note that the numerical setup in both cases is almost identical; the only difference is in the value of the wind stress, with $\tau = 0$ in InI simulations and $\tau = 1$ in EII simulations.

Because the initial interior viscous stress is zero (no vertical shear of the initial current), the EII case is equivalent to a “step response”, where the wind goes from zero to some finite value instantaneously at $t = 0$. The bottom boundary conditions, namely, at $z = -1$, for horizontal and vertical velocities are free-slip and rigid-lid, respectively. In the horizontal direction, we impose periodic boundary conditions.

We solve the equations of motion using Dedalus, a highly flexible computational framework suitable for optimal parallelized simulations that solves partial differential equations using spectral methods [29]. The computational domain consists of a Fourier basis with $n_x = 2048$ grid points in the horizontal direction and a Chebyshev basis with $n_z = 128$ grid points in the vertical direction. We use dealiasing scale factors of 3/2 for each axis. Our simulations use a fixed time step $\Delta t = 10^{-3}$ and a second-order, two-stage Runge-Kutta integrator. The total simulation time is $T_f = 40\pi$, that is, twenty inertial periods.

We conduct an analysis of the similarities and differences between InI and EII that result from variations in the minimum Rossby number, with $\mathrm{Ro}_{\min} \in \{-1.1, \ldots, -1.9\}$ increasing by 0.1 in each simulation. We keep the Ekman number constant, namely $\mathrm{Ek} = 10^{-3}$. Variations of this parameter would likely affect the vertical scale of each instability, but this work is focused on the comparison of other dynamical features. Finally, the numerical setup described above is characterized by a bulk Reynolds number $\mathrm{Re} = \mathrm{Ro}/(\delta^2\mathrm{Ek}) \approx 10^3$, where $\delta = H/L$ is the aspect ratio of the jet.

B. Growth rate and energetics

We calculate the growth rate of the perturbations in each instability, namely,

$$\sigma = \frac{1}{2}\frac{1}{\langle w^2\rangle}\frac{d\langle w^2\rangle}{dt}, \tag{4}$$

where $\langle\cdot\rangle$ represents an integral over the full volume.

In a homogeneous fluid, the total kinetic energy $K = \left\langle|\boldsymbol{v}|^2/2\right\rangle$ is also the total energy of the system. To evaluate how much of the total energy is dissipated due to InI and EII, we calculate the energy budget of the flow, namely,

$$\frac{d\left\langle K\right\rangle}{dt} = \underbrace{\mathrm{Ek}\left\langle\nabla^2(|\boldsymbol{v}|^2/2)\right\rangle}_{\text{Diffusion } \mathcal{D}} - \underbrace{\mathrm{Ek}\left\langle|\nabla\boldsymbol{v}|^2\right\rangle}_{\text{Dissipation } \varepsilon}, \tag{5}$$

where $\mathcal{D}$ and ε represent kinetic energy diffusion and dissipation, respectively. Note that because we calculate the energy budget over the full volume of the flow and owing to the boundary conditions, there is no contribution from the advective and pressure terms.

C. Near-Inertial Oscillations

Our periodic boundary conditions in the horizontal directions and background rotation allow for volume-averaged near-inertial oscillations of the horizontal velocity field. In order to better visualize the flow that is solely induced by the development of InI and EII, we remove the signal of such oscillations by plotting data in the frame of reference of the volume mean flow and subtracting such mean from the horizontal velocity field. In other words, we define the mean along-x displacement as $\hat{x} = \int_0^t \langle u\rangle dt'$. Then, at each time step, we interpolate our data into a primed frame of reference defined by $x' = x - \hat{x}$. Finally, we subtract the mean flow that comprises the oscillating flow from the horizontal velocity field to obtain $u' = u - \langle u\rangle$. Note that, by construction, the flow that we remove in this process is homogeneous in space. Given the absence of internal shear and the free-slip boundary conditions at the bottom, the removed oscillations diffuse and dissipate little to no energy, and therefore have little to no impact on the time-mean values of $\mathcal{D}$ and ε. They do introduce some oscillations in the time series in the case of EII as will be discussed below. Likewise, since the oscillations are confined to the horizontal plane, the calculation of σ is also unaffected by them. Note that we only apply this procedure to facilitate the reading of certain plots in which the oscillating flow could obscure other features of interest.

III. RESULTS

This section starts with a detailed analysis of a sample simulation characterized by $\mathrm{Ro}_{\min} = -1.5$. We select this value to allow for significant development of both InI and EII. Subsequently, we present our discussion around the effects on the dynamics and energetics of each instability resulting from variations of $\mathrm{Ro}_{\min}$, which is essentially the amplitude of the lateral shear of the initial current.

A. Sample case

1. Vertical Pumping

One of our main interests is the vertical velocity w induced by each instability, as it would be crucial for the vertical transport of physical properties in the ocean, particularly in the submesoscale. In Figure 2, we show snapshots of w at four different times that are selected to represent the onset, an intermediate stage, the weakening, and the return to a stable state of both InI and EII. Each panel also shows regions of marginally stable flow, where locally $-0.99 < \mathrm{Ro} < -0.7$, and unstable flow, where locally $\mathrm{Ro} < -1$. The contours of Ro seem to follow the structure of the vertical flow.

Several differences are immediately distinguishable. First, note from the time stamps that EII takes significantly less time than InI to start and then reach its maximum development, which is a direct consequence of the much faster initiation and development of the instability. Furthermore, panels (a)–(d) show that the magnitude of the pumping

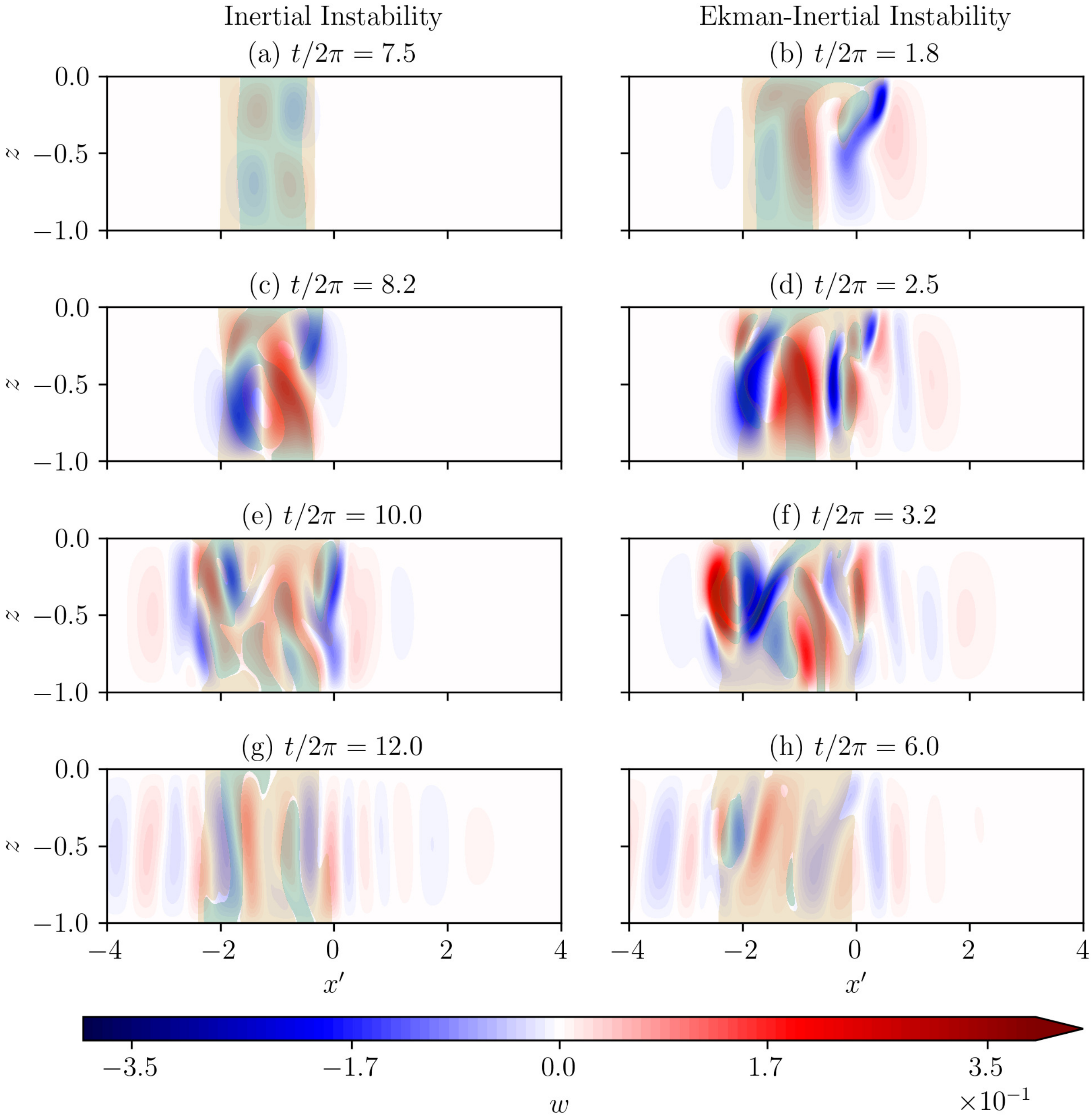

FIG. 2. Evolution of the vertical flow w (blue/red shades) induced by InI and EII at $\mathrm{Ro}_{\min} = -1.5$, visualized in the reference frame of the inertial oscillation. Translucent gold shades indicate marginally stable flow ($-0.99 < \mathrm{Ro} < -0.7$), and translucent turquoise indicate unstable flow ($\mathrm{Ro} < -1$).

induced by EII, hereafter called Ekman-Inertial pumping, is also larger than that of InI. In particular, panel (b) highlights that the Ekman-Inertial pumping is more intense near the surface, where the triggering stress is applied. We can also see from the gold and turquoise shades that fluid parcels closest to the surface are displaced the farthest, which is another distinctive feature of EII. On the other hand, as shown in panel (a), the vertical flow induced by InI exhibits a modal structure that is consistent with a normal mode two wavenumber, where the flow velocity magnitudes reach the maximum values around $z = -0.25$ and $z = -0.75$. Note from panels (e)–(h) that, at the end of both instabilities, wave packets are emitted away from the unstable regions.

To better visualize the time evolution of these waves, Figure 3 shows Hovmöller diagrams of w at $z = -0.5$. Despite

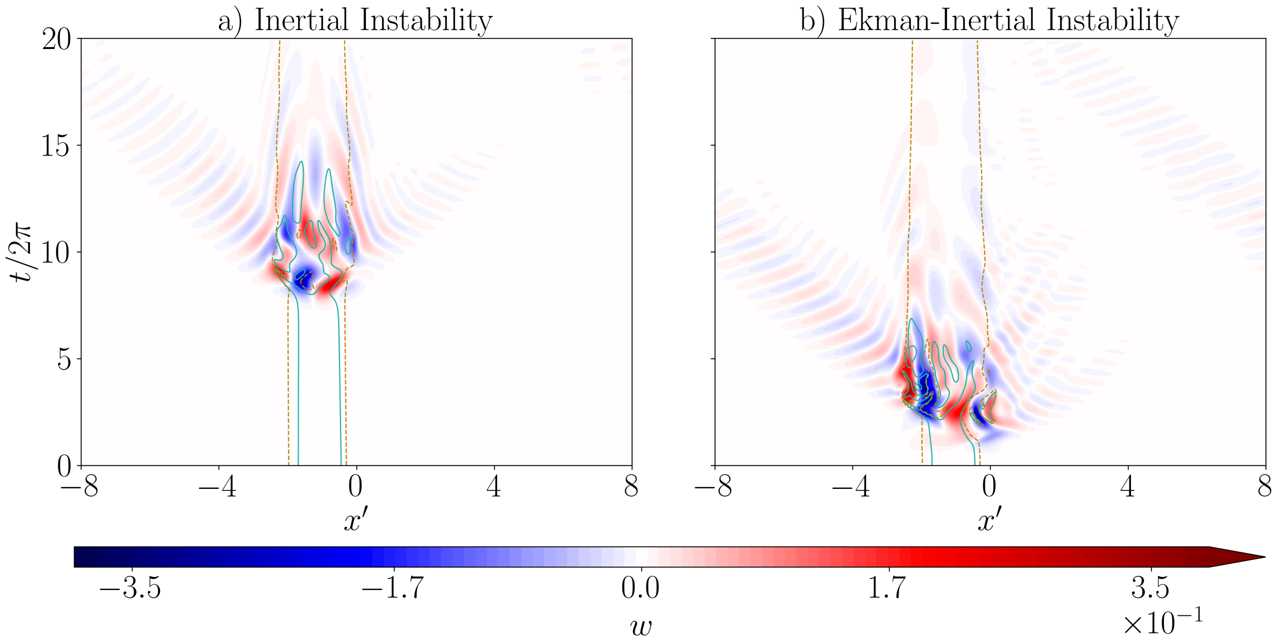

FIG. 3. Evolution of the vertical flow induced by InI and EII at $z = -0.5$ and for $\mathrm{Ro}_{\mathrm{min}} = -1.5$, visualized in the reference frame of the inertial oscillation. Contours of $\mathrm{Ro} = -0.7$ and $\mathrm{Ro} = -1$ are shown in gold (dashed line) and turquoise (solid line), respectively.

the fact that Ekman-Inertial pumping is stronger near the surface, we found that the fundamental features of the flow do not change significantly across different depths, so we choose a common level for both instabilities to facilitate the subsequent analyses.

Figure 3 shows that both instabilities radiate internal waves. They do so preferentially from the anticyclonic flanks, where the generating disturbance takes place. They also radiate preferentially away from this region, and are less likely to cross the cyclonic flank of the jet. We can form a hypothesis as to why by considering the dispersion relation of internal waves of angular frequency ω in a rotating, unstratified fluid such as ours. This relation is $\omega^2 = F^2 \sin^2\theta$, where $F = f\sqrt{1 + \mathrm{Ro}}$ is the effective Coriolis frequency, and θ is the angle of the phase planes with respect to the direction of the rotation vector. There are two conditions for this dispersion relation to accept propagating solutions: First, F must be real, i.e., $1 + \mathrm{Ro}$ must be positive and the flow stable. Second, we must have $\omega < F$, with $F > f$ ($F < f$) on the (anti)cyclonic flank of the jet, and $F = f$ outside of it. Therefore, the cyclonic flank traps waves for which $f < \omega < F$. On the anticyclonic flank, where the instability occurred, waves whose frequency is in the band $F < \omega < f$ tend to be expelled out of it, or to reflect off of it when propagating from elsewhere. Validating these hypotheses would require a detailed analysis of the interactions between the waves and the mean flow, which we reserve for future studies.

2. *Growth rate σ*

Figure 4 highlights the differences in temporal evolution of growth rate σ for InI and EII for the sample simulation as hinted by the Hovmöller diagrams of vertical pumping in Figure 3. Although both instabilities start with the same initial conditions, EII grows fast enough to significantly exceed the value of the inertial growth rate even at the first point of the timeseries. In the case of InI, the growth rate plummets to zero at $t/2\pi \approx 0.5$ to subsequently increase, until it saturates at $t/2\pi \approx 2$. Past this time, we have normal growth, during which the flow exhibits a modal structure (cf. Figure 2(a)) where all of its components grow in unison. This suggests that a transient growth behavior is observed for InI at $0 < t/2\pi \leq 2$, which is defined to be the intermediate state between the initial growth rate and the long-term growth rate (i.e., exponential normal mode growth rate) [26, 30]. Note that identifying a "transient growth rate" according to this definition is irrelevant for EII, since there is no modal long-term behavior. One could describe EII as a self-extinguishing form of transient growth, where different levels of the water column grow at different rates [27]. We can see this behavior in Figure 2(b), where the instability has grown first in the upper

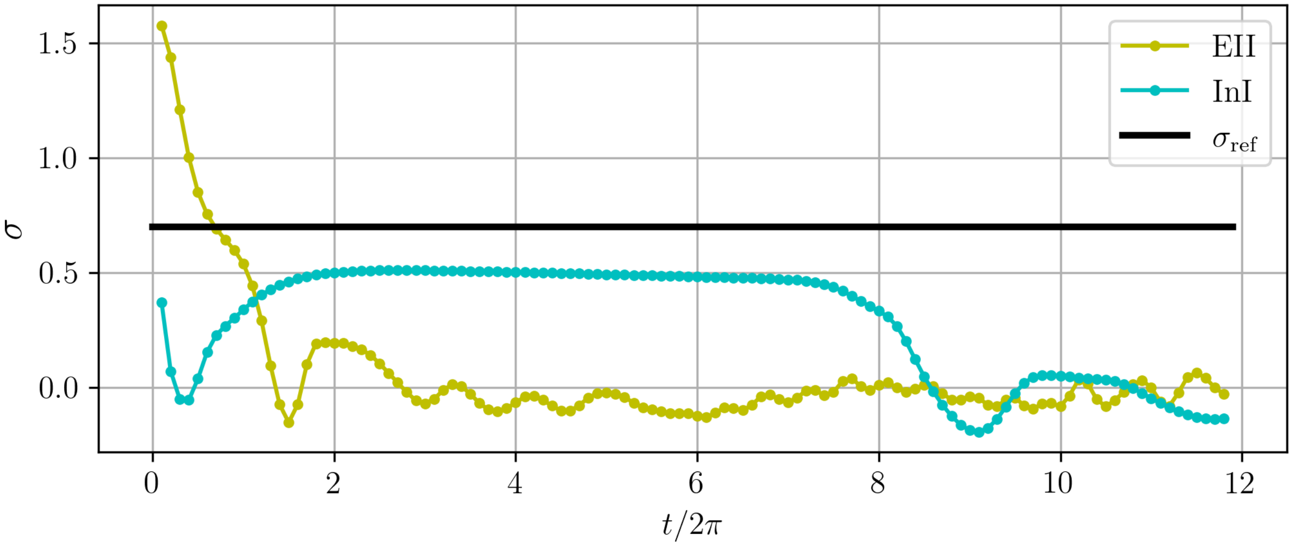

FIG. 4. Time series of the growth rate of InI and EII for the simulations with $\text{Ro}_{\text{min}} = -1.5$. The black line indicates the value of $\sigma_{\text{ref}} = f\sqrt{-1 - \text{Ro}_{\text{min}}}$.

layers, as shown by a downwelling that is more intense near the surface of the flow and shifted to the right, where the instability has advected it. Since the initial growth rate is generally larger than the normal mode growth rate, the transient growth rate is expected to decrease over time. However, in the case of EII, the growth rate decreases much slower over the initial period, thus allowing the rapid development of instabilities and strong vertical flow as seen in Fig. 2(b) and Fig. 3(b).

The growth rate of InI exceeds the growth rate of EII around $t/2\pi = 1.2$. At $t/2\pi \approx 2$, the InI growth rate reaches its maximum of about 0.5. Note that the growth rate of perturbations in an inviscid, infinite-domain shear would be $\sigma_{\text{ref}} = f\sqrt{-1 - \text{Ro}_{\text{min}}} \approx 0.7$. Previous studies [25, 28] of InI in a barotropic jet have found that, in flows with a finite Reynolds or Ekman number, i.e., in the presence of viscosity as in our case, the spatial structure of the fastest-growing mode and its associated growth rate depend on the value of Re (or Ek) and that of the aspect ratio of the jet $\delta = H/L$. In particular, the vertical wavenumber $k = 2\pi/H$ of the fastest-growing InI mode and its associated growth rate increase with Re. Likewise, the growth rate is a monotonically increasing function of the aspect ratio δ. In all cases, σ_{ref} is an upper bound for the value of the actual growth rate. Therefore, we attribute our lower InI growth rate compared to σ_{ref} to the presence of viscous effects, vertical boundaries, and the finite lateral extent of the jet. The growth rate then starts decreasing slightly due to the slow viscous diffusion of the jet but remains relatively constant, and perturbations grow exponentially, according to linear theory. The instability starts saturating at about $t/2\pi = 7.5$, past which it abruptly drops to zero. After this point, similarly to EII, the growth rate remains close to zero.

3. *Energetics*

The energy budget of the system is calculated as in Eq. (5) for InI and EII, and each term is individually plotted in Figure 5. As each instability develops, some kinetic energy is naturally lost to dissipation. Note that in both cases, the minimum of the energy rate of change is reached once the instabilities start to weaken, that is, after their growth rate has also reached its minimum (see Figure 4), allowing enough time for the flow to dissipate kinetic energy. The most remarkable difference, however, is in the diffusion term of the energy budget; although it is negligible in InI, it shows an oscillating behavior in EII. Such oscillations result from the combined effect of the wind stress applied at the surface and the near-inertial oscillation described in section II C. Indeed, the wind stress is applied by inducing vertical shear in the horizontal flow in the direction along the current, and the near-inertial oscillation is constantly changing direction, in particular along the current. Therefore, whenever the direction of the oscillation is the same (opposite) as the direction of the surface forcing, the diffusion of kinetic energy increases (decreases), resulting in a local maximum (minimum) in the diffusion curve of Figure 5. A similar response to surface winds was reported by Crawford and Large [31], in which an off-resonant interaction between inertial currents and steady-direction winds

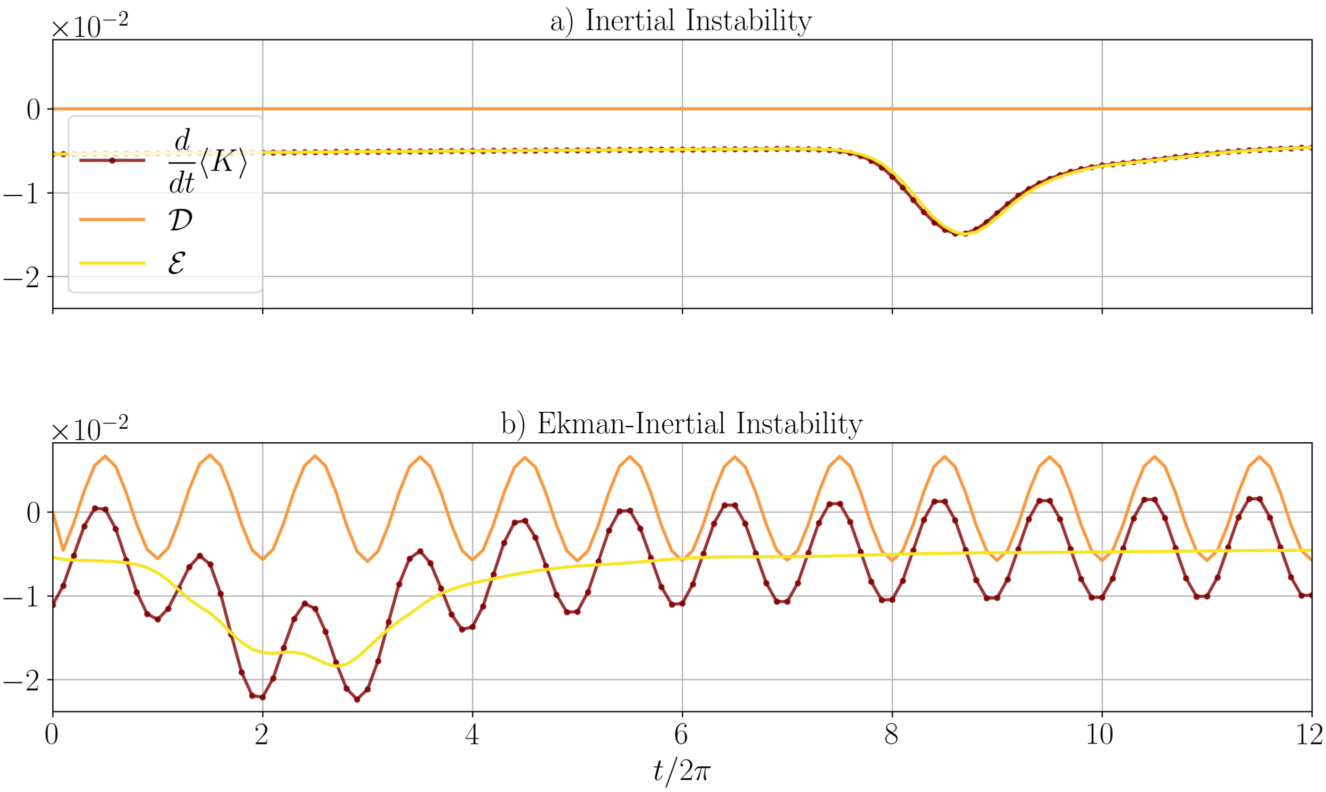

FIG. 5. Energy Budget of InI and EII at $\mathrm{Ro}_{\min} = -1.5$.

leads to a decrease in kinetic energy while a resonant interaction between inertial currents and winds rotating at the inertial frequency maximizes the kinetic energy.

Figure 6 shows the time-averaged spatial distribution of kinetic energy diffusion (panels (a) and (b)), as well as its horizontally-averaged temporal evolution (panels (c) and (d)). As expected, the first row of Figure 6 shows that kinetic energy is primarily diffused in the region around the jet for both InI and EII, and the diffusion caused by EII is particularly localized in the upper layers of the domain, where the wind stress continuously supplies momentum from above. On the other hand, panel (d) shows diffusion being alternately enhanced and diminished by the interaction between the near-inertial oscillations and the wind stress at the surface, while in panel (c), the absence of surface forcing leads to nearly negligible diffusion at the top of the domain.

4. Vorticity statistics

As both instabilities develop, the induced horizontal flow mixes cyclonic (stable) and anticylonic (unstable) flow, leading to changes in the vorticity field. In Figure 7, each histogram represents the distribution of the local Rossby numbers at different times over the course of the simulations. We exclude the range $-0.1 < \mathrm{Ro} < 0.1$ since the flanks of the current are characterized by $\mathrm{Ro} = 0$ at all times, but this is due to the Gaussian shape of the current, not the instabilities themselves. Note that the symmetry associated with the initial state of the current is eventually broken.

In the early stages of each instability, we observe a large peak at $\mathrm{Ro} = -1$. Over time, it shifts to a narrow peak around $-1 < \mathrm{Ro} < -0.7$, indicating that once the instabilities have subsided, much of the flow ends up close to the stability threshold. The main difference between the two is yet again in the timing: the process is much faster with EII than with InI, that is, stabilization occurs within $t/2\pi = 12$ in InI and $t/2\pi = 6$ in EII, which correspond to the times when kinetic energy rate of change reaches a steady state (Fig. 5) and the growth rate of perturbations is approximately zero (Fig. 4). After these times, we also do not find unstable flow in the Hovmöller diagrams of w (see turquoise lines in Fig. 3). Subsequently, both distributions remain in such a marginally stable state, with the EII maximum distribution slowly drifting towards higher values of Ro. While the post-instability evolution of the flow is beyond the scope of this work, we hypothesize that this drift is similar to the drift towards smaller values of Ro that we can see for the cyclonic distributions, and that these drifts are due to viscous diffusion smoothing out sharp

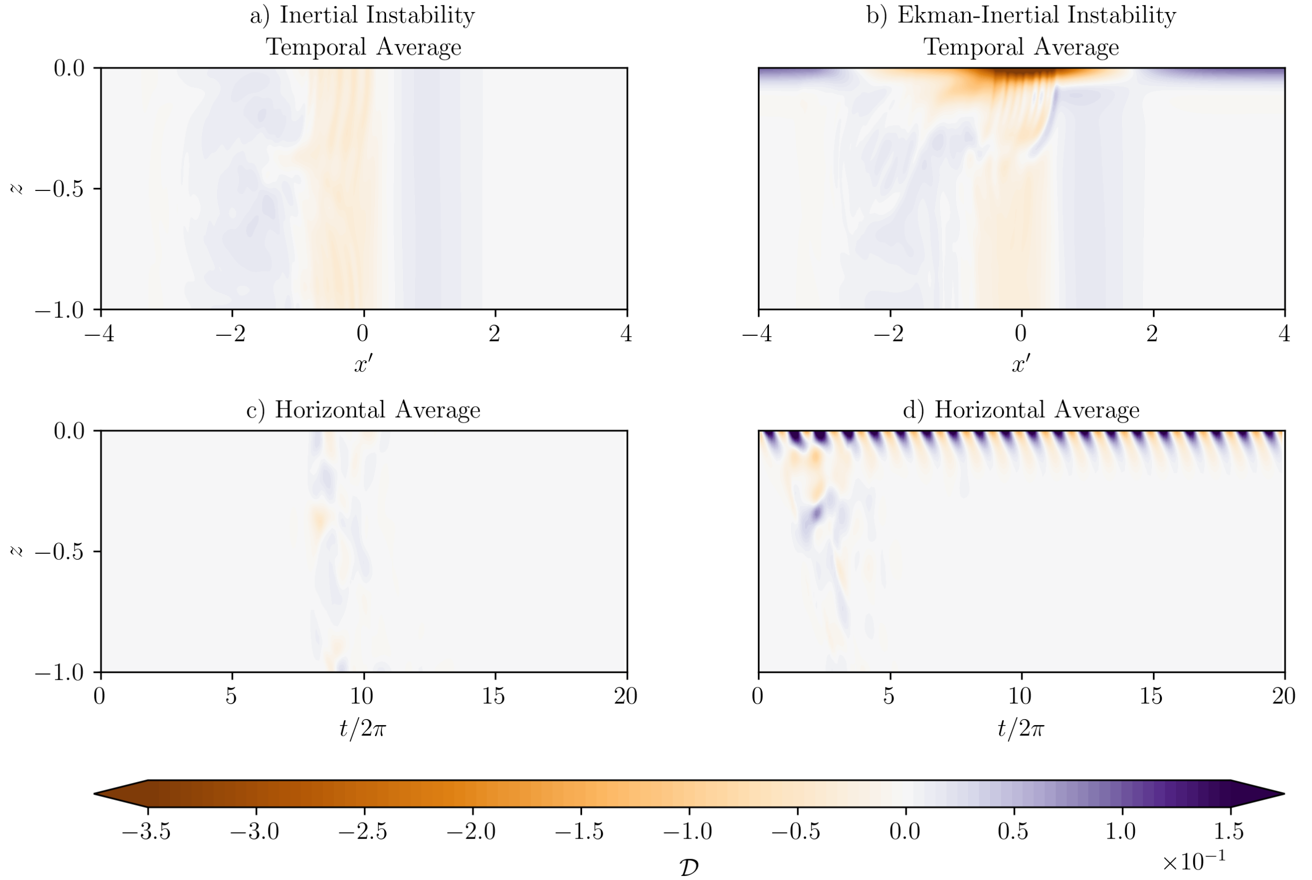

FIG. 6. Kinetic energy diffusion $\mathcal{D}$ over the course of evolution of InI and EII at $\mathrm{Ro_{min}} = -1.5$. (a,b) Temporally-averaged $\mathcal{D}$ over the entire simulation time and (c,d) spatially-averaged $\mathcal{D}$ over the entire horizontal domain.

velocity gradients.

B. Varying the minimal Rossby number

We investigate how the growth rates of EII and InI are affected by variations in $\mathrm{Ro_{min}}$, i.e., changes in lateral shear of the flow. Figure 8 shows a time series of the growth rates, each line corresponding to a different experiment. While defining the InI growth rate is more straightforward because of its long-term modal growth, it is not obvious what value should be selected to be the representative growth rate from the EII experiments. Time series curves in Figure 8 reveal that the EII growth rate is more akin to that of transient growth in that it has an inherent time dependence and does not have the single value corresponding to the fastest-growing normal mode long-term behavior. In our simulations for both InI and EII, the initial growth rate is due to the non-normality of the initial condition, and the value is the same because all simulations have the same noisy initialization. Across all $\mathrm{Ro_{min}}$ and for both InI and EII, the initial growth rate then reduces due to viscous forces at a similar rate for each instability type until $t/2\pi \approx 0.4$, indicated by the time series curves for each of InI- and EII-type simulations collapsing. Right after $t/2\pi = 0.4$, the InI growth rate is suppressed to zero, whereas the EII growth rate sustains significantly positive values across all simulations. We also note that the EII growth rates across the different values of $\mathrm{Ro_{min}}$ start diverging from each other around $t/2\pi = 0.5$, which could indicate the end of an initial "adjustment" stage similar to the transient growth stage of InI. Therefore, we define the time period $t/2\pi \leq 0.4$ as the initial transient state and do not consider it in our analysis. It is important to note that unlike InI, for which a long-term growth rate can be defined, EII growth rate continues to decrease to zero throughout the time series. A different time can be chosen to define the end of the initial transient period, but the results in terms of the EII growth rate sensitivity to $\mathrm{Ro_{min}}$ are qualitatively the same. For each $\mathrm{Ro_{min}}$, we define the growth rate of InI to be the maximum growth rate after this transient initial period, which reveals the modal growth rate corresponding to the flat regions of the time series. As mentioned above,

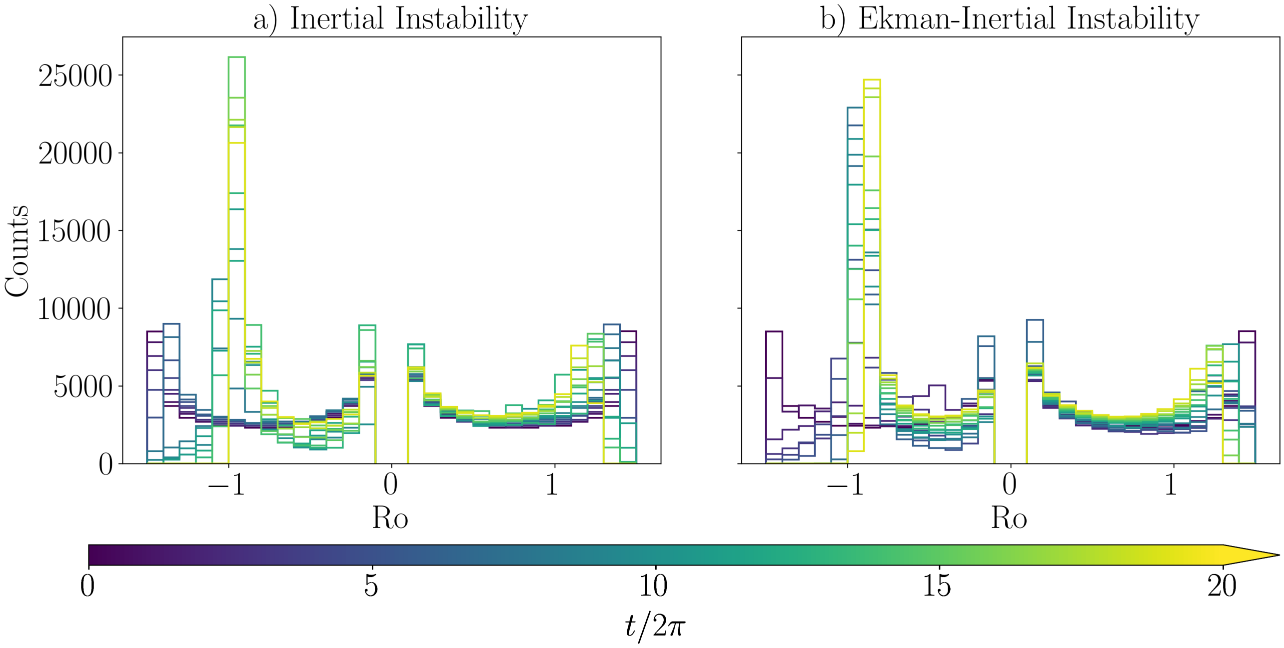

FIG. 7. Histograms of Ro at every inertial period, for a simulation with $\mathrm{Ro_{min}} = -1.5$. To facilitate visualization, we do not show the sampling corresponding to the range $-0.1 < \mathrm{Ro} < 0.1$.

defining a single value for EII growth rate is more complicated. In this paper, we choose the growth rate values at $t/2\pi = 0.5$, acknowledging that this choice is somewhat arbitrary.

Interestingly, while the qualitative behavior of the EII growth rate remains rather similar across different values of $\mathrm{Ro_{min}}$, the InI time series reveal a shorter phase of linear growth rate as $\mathrm{Ro_{min}}$ becomes more negative. The relative dependence on $\mathrm{Ro_{min}}$ is even more evident in Figure 9, which shows the maximum growth rate of each experiment as a function of $\mathrm{Ro_{min}}$. Additionally, we show the theoretical maximum growth rate of InI, σ_{ref}, predicted by linear stability analysis. Because of viscous forces, InI growth rate is less than σ_{ref} for all values of $\mathrm{Ro_{min}}$, similarly to what we observe in Figure 4. Notably, EII growth rate exceeds that of InI for all $\mathrm{Ro_{min}}$ by a factor of $1.5 - 6$ and even exceeds σ_{ref} except for in the case of our most unstable jet with $\mathrm{Ro_{min}} = -1.9$. The growth rates of both EII and InI increase with smaller (more unstable) $\mathrm{Ro_{min}}$, but InI maximum growth rate varies more with $\mathrm{Ro_{min}}$ than that of EII. Note that in EII, the imposed wind stress acts as the main triggering perturbation, and hence its growth rate might be more sensitive to other factors, such as the viscous forces responsible for its propagation.

IV. DISCUSSION AND CONCLUSIONS

The results of our idealized two-dimensional simulations qualitatively agree with some of the predictions by Grisouard and Zemskova [27], showing a significantly faster growth rate of EII compared to the growth rate of InI. Even though we find that EII growth rate exceeds that of InI by a factor of $1.5-6$, not by orders of magnitude as expected from the one-dimensional study [27], this primary difference still has dynamical consequences that become apparent in 2D, such that perturbations induce both horizontal and vertical flows that lead to turbulent motions and eventually extinguish the instability. The main conclusions of this work can be summarized as follows:

- EII grows faster than InI in the case of our step response to wind stress. The growth rate of EII is more time-dependent in contrast with a more easily identifiable long-term modal growth rate of InI.
- EII induces stronger horizontal and vertical flows and does so much earlier than InI.
- In both cases, the induced vertical flow is fast and strong enough to radiate inertial waves.
- In both instabilities, kinetic energy is lost to viscous dissipation and the emitted wave field. Additionally, the continuous surface forcing applied in EII diffuses kinetic energy throughout the entire simulation, but it does not significantly affect the global energy budget.

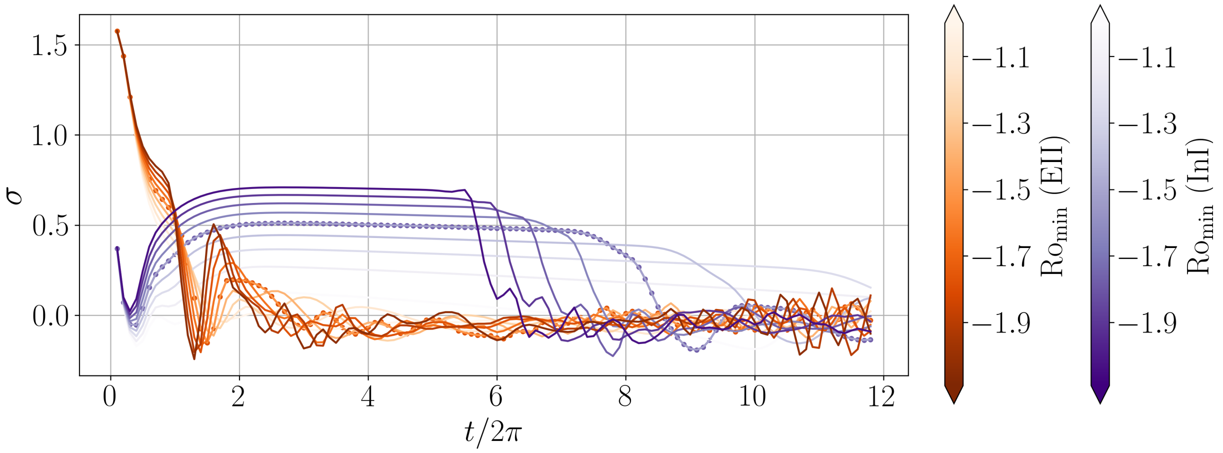

FIG. 8. Time series of growth rates for experiments with different $\mathrm{Ro}_{\mathrm{min}}$. We use markers to identify the time series from our sample $\mathrm{Ro}_{\mathrm{min}} = -1.5$ case and different colorbars to distinguish between the InI and EII experiments.

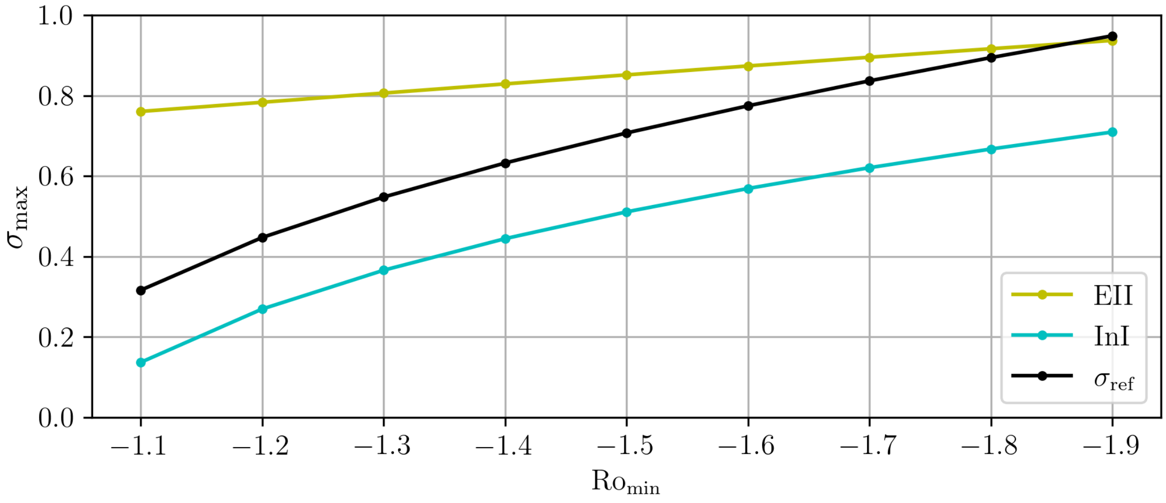

FIG. 9. Maximum growth rate for each instability, calculated after the transient state ($t/2\pi \geq 0.5$), as function of $\mathrm{Ro}_{\mathrm{min}}$. The black line corresponds to $\sigma_{\mathrm{ref}} = f\sqrt{-1 - \mathrm{Ro}_{\mathrm{min}}}$.

- EII manifests itself preferentially near the surface, while InI does so in the interior of the flow.
- Both instabilities reach a similar stable state, where most of the flow tends to remain close to the instability threshold $\mathrm{Ro} = -1$. This process occurs faster in EII than in InI.

In short, despite their common features, EII and InI have substantial differences that were not obvious from the one-dimensional analysis of Grisouard and Zemskova [27]. There are also important effects that our setup is not capturing, such as variations in the direction along the current and three-dimensional turbulence. Nevertheless, our work provides valuable information on the circulation induced in a plane across the current that results in vertical transport of ocean properties and can be more significant in EII than the one reported for other submesoscale instabilities.

Another limitation of our study is the assumption of homogeneous fluid, which is motivated by our focus on EII, whose main sources of kinetic energy are the lateral shear of the geostrophic current and the vertical shear provided by the surface forcing. This setup is also representative of the near-surface ocean mixed layer, where submesoscale instabilities are important. While this allows us to reveal the most basic dynamics of EII, a stratified environment would permit other submesoscale processes such as frontogenesis [32], mixed layer instabilities [16], or gravitational and/or symmetric instabilities [18]. Their effects might interfere with those of EII, resulting in either an enhancement or a reduction of vertical stratification and vertical velocities in the upper ocean. Nonetheless, Grisouard and Zemskova [27] suggest that, even in the presence of stratification, EII could grow faster and dominate over other submesoscale baroclinic instabilities. They also propose that EII could advect lateral density gradients like passive tracers and have a direct impact on the potential energy budget of a front. This is consistent with results from Grisouard [22], in which changes in the kinetic and potential energy of density fronts could not be explained by symmetric instability, even when it was supposed to dominate. Instead, the simulations featured unexpected strong signs of InI, as well as leading-order variations in the potential energy budgets of the fronts. In hindsight, those could have been signs of EII.

For simplicity, we only consider the case of a constant wind stress along the current that starts at $t = 0$, or "infinitely" quickly, and is sustained throughout the simulation. Our motivation is that wind conditions can change much faster than surface currents, and trigger an EII-induced flow much faster than InI that grows in the interior of the domain. Nevertheless, how abrupt the surface forcing must be in order to trigger EII, and for it to outcompete InI or any of the aforementioned instabilities should be further investigated, as well as the sensitivity of EII to changes in the magnitude and direction of the wind.

In this study, we keep the Ekman number constant, which in dimensional quantities translates into keeping a fixed eddy viscosity ν. Since viscous fluxes are responsible for propagating the surface perturbation into the interior in the case of EII, we would expect variations in Ek to impact the vertical extent of the induced flow and its corresponding ability to dissipate kinetic energy. In this case, InI may become dominant below a "critical" depth given that it already starts within the interior of the flow. Such a hypothesis is testable using the configuration presented here, but is not the focus of this work.

The internal waves generated by both instabilities are of special interest. As shown in Figure 3, the most intense pumping is not centered in the domain. Instead, it develops mainly within the anticyclonic region, where the propagation of radiated waves is also enhanced, especially in EII. We can compare this situation with stratified, rotating flows where the buoyancy frequency N is significantly larger than f. This situation is commonly observed deeper in the ocean, in fronts and eddies with small Rossby numbers. There, internal waves can only propagate if $F < \omega < N$, which implies the following differences between the strongly stratified case and ours. To begin with, in the stratified case, (anti)cyclonic vorticity raises (lowers) the lower bound of the propagative band locally, but its upper bound remains N. In our unstratified case, (anti)cyclonic vorticity raises (lowers) the upper bound of the propagating band, while the lower bound remains zero. Consequently, in the stratified case, regions of (anti)cyclonic vorticity expel waves for which $f < \omega < F$ (trap waves for which $F < \omega < f$) [33, 34]. Conversely, in our unstratified case, within the same frequency band, regions of (anti)cyclonic vorticity trap (expel) waves. By definition, the oceanic mixed layer tends to be well-mixed, with spatiotemporal variations. For example, it is more mixed at night, due to convective cooling, or during weather events. Whether internal waves propagate in a strongly stratified fluid or not must be determined on a case-by-case basis.

The fact that both instabilities emit internal waves shows that kinetic energy is exchanged between the original current that is initially in geostrophic balance and the wave field. A thorough analysis of such energetic interactions requires separating the balanced flow from the wave field, which can be achieved using several techniques, but is still a challenging task in fluid dynamics. Therefore, we will reserve the implementation of a Lagrangian filter that allows us to accurately conduct this separation and investigate the corresponding wave-mean flow interactions for a future study.

Finally, we wish to reiterate that our study aims to characterize the most basic dynamical features of EII by comparing it with InI. Although submesoscale instabilities have been directly measured in the past [15, 20, 35, 36], comparing the results presented here with observational data may be a premature step, given that our current understanding of EII is still relatively shallow. Therefore, we prefer to reserve such comparisons for future studies. Intermediate steps could consist in numerical studies that use a less idealized setup, for example, three-dimensional large-eddy simulations.

Data Availability Statement

The code that supports this article can be found at [37].

ACKNOWLEDGMENTS

Computations were performed on the Béluga supercomputer located at the École de Technologie Supérieure in Montreal. F.T.J. acknowledges the financial support of the Consejo Nacional de Humanidades, Ciencias y Tecnologías (CONAHCYT) [doctoral scholarship number 774000]. F.T.J. and N.G. acknowledge the financial support of the Natural Sciences and Engineering Research Council of Canada (NSERC), [funding reference numbers RGPIN-2015-03684 and RGPIN-2022-04560]. V.E.Z. acknowledges the following National Science Foundation grants: OCE-1756752, OCE-2220439, and OCE-2319609.

[1] P. Klein, G. Lapeyre, L. Siegelman, B. Qiu, L.-L. Fu, H. Torres, Z. Su, D. Menemenlis, and S. Le Gentil, Ocean-scale interactions from space, Earth and Space Science **6**, 795 (2019).

[2] J. R. Taylor and A. F. Thompson, Submesoscale dynamics in the upper ocean, Annual Review of Fluid Mechanics **55**, 103 (2023).

[3] J. C. McWilliams, Submesoscale currents in the ocean, Proceedings of the Royal Society A: Mathematical, Physical and Engineering Sciences **472**, 20160117 (2016).

[4] L. Siegelman, Energetic submesoscale dynamics in the ocean interior, Journal of Physical Oceanography **50**, 727 (2020).

[5] Z. Su, J. Wang, P. Klein, A. F. Thompson, and D. Menemenlis, Ocean submesoscales as a key component of the global heat budget, Nature Communications **9**, 1 (2018).

[6] K. M. Smith, P. E. Hamlington, and B. Fox-Kemper, Effects of submesoscale turbulence on ocean tracers, Journal of Geophysical Research: Oceans **121**, 908 (2016).

[7] M. Lévy, R. Ferrari, P. J. S. Franks, A. P. Martin, and P. Rivière, Bringing physics to life at the submesoscale, Geophysical Research Letters **39** (2012).

[8] M. Lévy, P. J. Franks, and K. S. Smith, The role of submesoscale currents in structuring marine ecosystems, Nature Communications **9**, 4758 (2018).

[9] A. Mahadevan, The impact of submesoscale physics on primary productivity of plankton, Annual Review of Marine Science **8**, 161 (2016).

[10] J. R. Taylor and R. Ferrari, Ocean fronts trigger high latitude phytoplankton blooms, Geophysical Research Letters **38** (2011).

[11] Z. Jing, B. Fox-Kemper, H. Cao, R. Zheng, and Y. Du, Submesoscale fronts and their dynamical processes associated with symmetric instability in the northwest pacific subtropical ocean, Journal of Physical Oceanography **51**, 83 (2021).

[12] A. C. N. Garabato, X. Yu, J. Callies, R. Barkan, K. L. Polzin, E. E. Frajka-Williams, C. E. Buckingham, and S. M. Griffies, Kinetic energy transfers between mesoscale and submesoscale motions in the open ocean's upper layers, Journal of Physical Oceanography **52**, 75 (2022).

[13] R. Ferrari and C. Wunsch, Ocean circulation kinetic energy: Reservoirs, sources, and sinks, Annual Review of Fluid Mechanics **41**, 253 (2009).

[14] L. N. Thomas, A. Tandon, and A. Mahadevan, Submesoscale processes and dynamics, in *Ocean Modeling in an Eddying Regime* (American Geophysical Union (AGU), 2008) pp. 17–38.

[15] A. Y. Shcherbina, E. A. D'Asaro, C. M. Lee, J. M. Klymak, M. J. Molemaker, and J. C. McWilliams, Statistics of vertical vorticity, divergence, and strain in a developed submesoscale turbulence field, Geophysical Research Letters **40**, 4706 (2013).

[16] G. Boccaletti, R. Ferrari, and B. Fox-Kemper, Mixed layer instabilities and restratification, Journal of Physical Oceanography **37**, 2228 (2007).

[17] J. R. Taylor and R. Ferrari, Buoyancy and wind-driven convection at mixed layer density fronts, Journal of Physical Oceanography **40**, 1222 (2010).

[18] L. N. Thomas, J. R. Taylor, R. Ferrari, and T. M. Joyce, Symmetric instability in the gulf stream, Deep Sea Research Part II: Topical Studies in Oceanography **91**, 96 (2013), subtropical Mode Water in the North Atlantic Ocean.

[19] J. Gula, M. J. Molemaker, and J. C. McWilliams, Submesoscale cold filaments in the gulf stream, Journal of Physical Oceanography **44**, 2617 (2014).

[20] J. Callies, R. Ferrari, J. M. Klymak, and J. Gula, Seasonality in submesoscale turbulence, Nature Communications **6**, 6862 (2015).

[21] L. Brannigan, D. P. Marshall, A. C. N. Garabato, A. J. G. Nurser, and J. Kaiser, Submesoscale instabilities in mesoscale eddies, Journal of Physical Oceanography **47**, 3061 (2017).

[22] N. Grisouard, Extraction of potential energy from geostrophic fronts by inertial–symmetric instabilities, Journal of Physical Oceanography **48**, 1033 (2018).

[23] V. Verma, H. T. Pham, and S. Sarkar, The submesoscale, the finescale and their interaction at a mixed layer front, Ocean Modelling **140**, 101400 (2019).

[24] T. W. N. Haine and J. Marshall, Gravitational, symmetric, and baroclinic instability of the ocean mixed layer, Journal of Physical Oceanography **28**, 634 (1998).

[25] G. F. Carnevale, R. C. Kloosterziel, and P. Orlandi, Inertial and barotropic instabilities of a free current in three-dimensional rotating flow, Journal of Fluid Mechanics **725**, 117–151 (2013).

[26] V. E. Zemskova, P.-Y. Passaggia, and B. L. White, Transient energy growth in the ageostrophic eady model, Journal of Fluid Mechanics **885**, A29 (2020).

[27] N. Grisouard and V. E. Zemskova, Ekman-inertial instability, Phys. Rev. Fluids **5**, 124802 (2020).

[28] M. W. Harris, F. J. Poulin, and K. G. Lamb, Inertial instabilities of stratified jets: Linear stability theory, Physics of Fluids **34**, 084102 (2022).

[29] K. J. Burns, G. M. Vasil, J. S. Oishi, D. Lecoanet, and B. P. Brown, Dedalus: A flexible framework for numerical simulations with spectral methods, Phys. Rev. Res. **2**, 023068 (2020).

[30] S. Kimura, Initial and transient growth of symmetric instability, Journal of Physical Oceanography **54**, 115 (2024).

[31] G. B. Crawford and W. G. Large, A numerical investigation of resonant inertial response of the ocean to wind forcing, Journal of Physical Oceanography **26**, 873 (1996).

[32] J. C. McWilliams, Oceanic frontogenesis, Annual Review of Marine Science **13**, 227 (2021).

[33] C. N. K. Mooers, Several effects of a baroclinic current on the cross–stream propagation of inertial–internal waves, Geophysical Fluid Dynamics **6**, 245 (1975).

[34] E. Kunze, Near-inertial wave propagation in geostrophic shear, Journal of Physical Oceanography **15**, 544 (1985).

[35] A. F. Thompson, A. Lazar, C. Buckingham, A. C. N. Garabato, G. M. Damerell, and K. J. Heywood, Open-ocean submesoscale motions: A full seasonal cycle of mixed layer instabilities from gliders, Journal of Physical Oceanography **46**, 1285 (2016).

[36] M. Archer, A. Schaeffer, S. Keating, M. Roughan, R. Holmes, and L. Siegelman, Observations of submesoscale variability and frontal subduction within the mesoscale eddy field of the tasman sea, Journal of Physical Oceanography **50**, 1509 (2020).

[37] F. Trujano-Jimenez, fabiola-tj/2d-ekman-inertial-instability (2025).